Proceedings of ASME 2011 5th International Conference on Energy Sustainability & 9th Fuel Cell Science, Engineering and Technology Conference
ESFuelCell2011
August 7-10, 2011, Washington, DC, USA

ESFuelCell2011-54497

A FLUX MAPPING METHOD FOR CENTRAL RECEIVER SYSTEMS

Clifford K. Ho[1] and Siri S. Khalsa[2]
[1]Concentrating Solar Technologies Department, Sandia National Laboratories, P.O. Box 5800, Albuquerque, NM 87185-1127, USA, (505) 844-2384, ckho@sandia.gov
[2]Sandia Staffing Alliance, P.O. Box 5800, Albuquerque, NM 87185-1127, USA

ABSTRACT

A new method is described to determine irradiance distributions on receivers and targets from heliostats or other collectors for concentrating solar power applications. The method uses a CCD camera, and, unlike previous beam characterization systems, it does not require additional sensors, calorimeters, or flux gauges on the receiver or target. In addition, spillage can exist (the beam does not need to be contained within the target). The only additional information required besides the digital images recorded from the CCD camera is the direct normal irradiance and the reflectivity of the receiver. Methods are described to calculate either an average reflectivity or a reflectivity distribution for the receiver using the CCD camera. The novel feature of this new PHLUX method is the use of recorded images of the sun to scale both the magnitude of each pixel value and the subtended angle of each pixel. A test was performed to evaluate the PHLUX method using a heliostat beam on the central receiver tower at the National Solar Thermal Test Facility in Albuquerque, NM. Results showed that the PHLUX method was capable of producing an accurate flux map of the heliostat beam with a relative error in the peak flux of 2%.

1. INTRODUCTION

Monitoring the flux distribution of concentrated sunlight from heliostats (or other collectors) on receivers is important to maximize the optical and thermal performance of concentrating solar power systems. This paper presents a method to obtain flux maps on arbitrary (non-planar) surfaces using digital photography without the need for additional gauges on the receiver or target. Previous methods have employed beam characterization systems that required flat, water-cooled panels or moving "wands" with flux gauges for calibration and scaling of digital images. Other requirements of past methods included the need for the entire beam to fit within the target so that the total power, which was calculated from the size, orientation, and reflectivity of the collector, could be used to scale the pixel values to a flux (irradiance) magnitude. If spillage occurred (i.e., from a large array of heliostats or facets), this method could not be used. Infrared cameras have also been proposed to monitor the concentrated solar flux on the receiver, but the measured infrared radiation is dependent on the surface temperatures, which are dependent on uncertain factors such as the amount of heat absorbed by the heat transfer fluid and thermal losses from convection (wind) and radiation.

The current method of obtaining flux maps overcomes these shortcomings and employs just a few requirements: digital images of the illuminated receiver and of the sun, a current reading of the direct normal irradiance (DNI), and the receiver reflectivity. The image of the sun serves two purposes: (1) it provides a reference image so that pixel values of the receiver image can be scaled to a flux value (using the DNI reading) and (2) it provides a size reference to quantify the subtended angle (and size) of the receiver image. The reflectivity distribution of the receiver is characterized using comparative images with and without a beam of known power on the receiver, or by using a coupon of know reflectivity in the field of view of the receiver image. This paper presents the methodology and formulation that produce the flux maps from the digital images. The formulation also accounts for perspective views and for non-planar (e.g., cylindrical) receivers. Preliminary tests are presented to illustrate the method.

2. EXISTING FLUX MAPPING METHODS

Previous methods have used CCD (charge-coupled device) cameras and digital imaging methods to characterize irradiance distributions (or flux maps) from individual heliostat beams

and dish concentrators [1]-[4]. These traditional methods require a water-cooled flux gauge or calorimeter that is used to scale all pixel values in the digital image to the measured irradiance at a single location. The calibration and measurement of the flux gauge have been shown to provide the greatest source of uncertainty and error in the measured flux distribution [2].

Ulmer et al. [5] describe a similar method using a CCD camera to measure the flux distribution from a dish concentrator, but instead of using a flux gauge or calorimeter, they calculate the total power from the dish collector and use that to calibrate the pixel values. This method requires that the entire beam is captured by the target. For cases where spillage from the target occurs (e.g., large heliostat fields aimed at a central receiver), this method is not appropriate.

Slack et al. [6] describe a method that uses video cameras to determine flux distributions on eSolar's external receiver panels. The total power incident on a receiver panel is estimated using measurements of absorbed power (from the heat transfer fluid) and estimates of thermal losses. The estimated total incident power is then used to scale the pixel values in the video images. Although the issue of spillage is overcome, uncertainties exist in the measurements of absorbed power and thermal losses.

Yogev et al. [7] developed a flux scanner that can measure the irradiance distribution from an entire heliostat field. Flux sensors were contained in a long "wand" that rotated in front of the eSolar cavity receiver. A remote video camera was used to capture images of the reflected irradiance from the wand as it rotated, and the sensors were used to calibrate the pixel values corresponding to the Lambertian surface of the wand. The resulting images that were recorded while the wand rotated in front of the receiver were stitched together to yield a flux map of the irradiance distribution at the aperture of the cavity receiver. The authors discuss numerous mechanical and electronic challenges associated with this complex device.

Naor et al. [8] discuss the development of a flux measurement system using an infrared camera to measure the surface temperature of a central receiver and infer the irradiance distribution. However, many parameters and processes must be known to calculate the flux map: thermodynamic properties of the fluid in the receiver pipes, properties of the material comprising the pipes, and heat losses due to radiation and convection. Uncertainty in the parameters and processes, and associated parameters that impact these processes such as ambient temperature and wind speed, will contribute to uncertainties in the calculated flux distribution.

3. PHOTOGRAPHIC FLUX MAPPING – THE PHLUX METHOD

In this paper, we describe a simple method to obtain flux maps using a CCD-based camera that overcomes deficiencies described in the previous methods. The current method does not require additional sensors, calorimeters, or flux gauges on the receiver or target. The method can accommodate high solar fluxes and spillage from large heliostat fields. The only additional information required besides the recorded raw digital images or video is the direct normal irradiance (DNI, which is typically recorded at solar power plants) and the reflectivity of the target or receiver. Simple methods to accurately determine the reflectivity are described in Section 3.2.

As with other digital flux mapping methods, digital images of the concentrated (reflected) irradiance on the target or receiver are captured using a CCD camera (or video recorder). A unique feature of the PHLUX method is the use of recorded images of the sun to calibrate both the magnitude of each pixel value and the subtended angle of each pixel [9]. Neutral-density filters are applied to the camera lens to prevent saturation of the CCD during exposure. The reference images of the sun serve two purposes: (1) they provide a quantified irradiance reference so that pixel values can be scaled to power (watts) using the known DNI, and (2) they provide a spatial reference to quantify the subtended angle (and size) of the physical image. The subtended angle of the sun is ~9.4 mrad, so as long as the zoom is held constant, the subtended angle of other images can be obtained by comparison to the image of the sun. These images are then processed using an image processing code (i.e., Matlab) to determine the measured irradiance. The following sections describe the calculation of the target/receiver irradiance from recorded pixel values using the sun as a calibration. Perspective viewing, spatial scaling, and calculation of target/receiver reflectivity are also discussed.

3.1 Pixel Conversion Using Sun Calibration

Consider one square pixel, i, on a raw grayscale CCD image of a receiver. This pixel captures an elemental portion of the receiver, $A_{R,i}$ [m^2], which receives an irradiance, $E_{R,i}$ [W/m^2], from the heliostat field or other concentrator (Figure 1). The receiver element is assumed to be a Lambertian (diffuse) reflector with reflectivity, $\rho_{R,i}$.

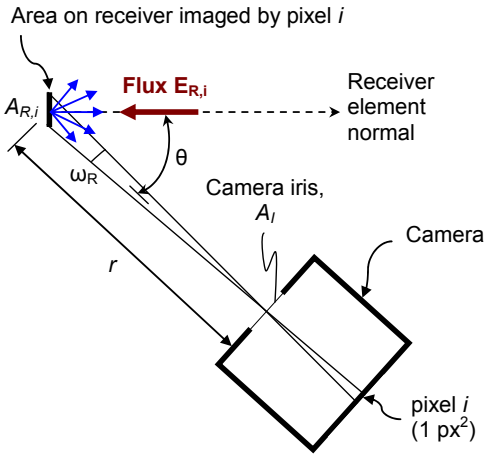

Figure 1. Reflection of irradiance on a small portion of a diffuse receiver toward a CCD camera. The area on the receiver, $A_{R,i}$, corresponds to the area captured by one pixel on the CCD.

The CCD response due to irradiance at this pixel is expressed in arbitrary voltage units per pixel area, $V_{CCD,i}$ [volts/px^2], where volts represents the pixel value and px denotes the unit length of a pixel. We wish to convert this recorded signal, $V_{CCD,i}$, to the receiver irradiance, $E_{R,i}$ [W/m^2], incident on the surface area of the receiver, $A_{R,i}$ [m^2], imaged by pixel *i*. An equation for the receiver irradiance can be derived by first considering the irradiance incident on the CCD. By definition, the radiant intensity [W/sr] from a diffuse reflection is directly proportional to the cosine of the angle between the surface normal and the observer's line of sight. Therefore, the irradiance on the pixel, E_{CCD_W} [W/px^2], is given by:

$$E_{\mathrm{CCD\_W}} = \frac{I_N \cos(\theta)\,\mathrm{d}\Omega}{1\,\mathrm{px}^2} \tag{1}$$

where I_N is the radiant intensity reflected *normal* to the receiver [W/sr], θ is the angle between the surface normal of the receiver element and the camera, dΩ is the solid angle subtended by the camera iris at the receiver element [sr] (Figure 2), and px is the unit length of a square pixel.

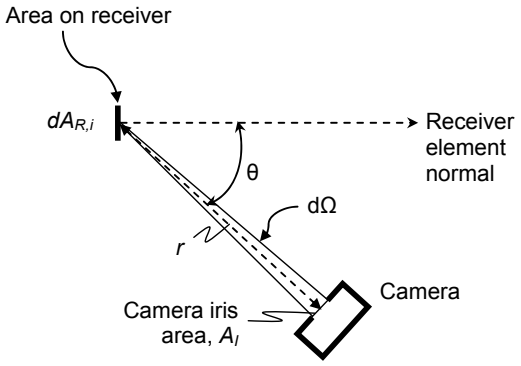

Figure 2. Solid angle, dΩ, subtended by the camera iris at the receiver element.

The radiant intensity in the normal direction, I_N [W/sr], in Eq. (1) is calculated by noting that all power reflected by surface A_R is reflected into a hemisphere, where ϕ is the zenith angle and α is the azimuth angle:

$$\begin{aligned}\rho_{R,i} E_{R,i} A_{R,i} &= \iint_{\text{Hemisphere}} I_N \cos(\theta)\mathrm{d}\Omega \\ &= I_N \int_0^{2\pi}\int_0^{\pi/2} \cos(\theta)\sin(\theta)\,d\theta\,d\phi \\ &= \pi I_N \\ \Rightarrow I_N &= \frac{\rho_{R,i} E_{R,i} A_{R,i}}{\pi}\end{aligned} \tag{2}$$

The solid angle, dΩ [sr], in Eq. (1) can be determined assuming that the radius of the camera iris is small compared to r [m], which is the distance between the receiver and the camera:

$$d\Omega(\mathrm{sr}) = \frac{A_I(\mathrm{m}^2)}{r^2(\mathrm{m}^2)} \tag{3}$$

where A_I [m^2] is the area of the camera iris. Substituting Eqs. (2) and (3) into Eq. (1) yields the following equation for the pixel irradiance [W/px^2]:

$$E_{CCD\_W} = \frac{\rho_{R,i} E_{R,i} A_{R,i} \cos(\theta) A_I}{\pi r^2 (1\,\mathrm{px}^2)} \tag{4}$$

The pixel irradiance in Eq. (4) [W/px^2] can be expressed in terms of the CCD response, $V_{CCD,i}$ [volts/px^2] by using a conversion factor between watts and volts. In order to obtain the conversion factor between watts and volts, an image of the sun is recorded using the same camera, zoom, and f-stop that was used for the image of the receiver. The W/volt ratio is equal to the ratio of the power that entered the camera in the sun image to the sum of the pixel values (volts) within the sun image:

$$\frac{\mathrm{W}}{\mathrm{volt}} = \frac{E_{\mathrm{DNI}} A_I}{\sum_{\mathrm{sun}} V_{CCD\_sun,i}} \tag{5}$$

where E_{DNI} [W/m^2] is the direct normal irradiance at the time the sun image was recorded, A_I [m^2] is the area of the camera iris, and $V_{CCD\_sun,i}$ is the CCD value of pixel *i* in the sun image. Dividing Eq. (4) by Eq. (5) yields the following equation for the CCD response, $V_{CCD,i}$ [volts/px^2] (note that the camera iris area, A_I, cancels out):

$$V_{CCD,i} = \frac{\rho_{R,i} E_{R,i} A_{R,i} \cos(\theta)}{\pi r^2 (1\ \mathrm{px}^2)} \frac{\sum_{\mathrm{sun}} V_{CCD\_sun,i}}{E_{DNI}} \tag{6}$$

The receiver element area, $A_{R,i}$ [m^2] in Eq. (6) can be expressed as follows (see Figure 1):

$$A_{R,i} \cos(\theta) = 4r^2 \tan^2(\omega_R / 2) \tag{7}$$

where r [m] is the distance between the receiver element and the camera iris, θ [rad] is the angle between the surface normal of the receiver element and the camera line of sight, and ω_R [rad] is the angle subtended from the camera iris to the receiver element (and spanned by one pixel). Assuming that the focal length (zoom) between the nodal point of the camera and the CCD is kept constant, an expression for ω_R can be determined by using the sun image as a reference for images/angles projected between the nodal point and the CCD (see Figure 3):

$$\frac{\tan(\omega_R/2)}{1/2\,\mathrm{px}} = \frac{\tan(\gamma/2)}{r_{\mathrm{sun\_pixels}}} \tag{8}$$

where r_{sun_pixels} is the number of CCD pixels along the radius of the sun image, and γ is the angle subtended by the sun

[~0.0093 rad]. Note that γ can vary by ~3% depending on the day of the year (distance between the sun and earth; see Appendix for additional details). Atmospheric effects and scattering may also impact the perceived subtended angle of the sun.

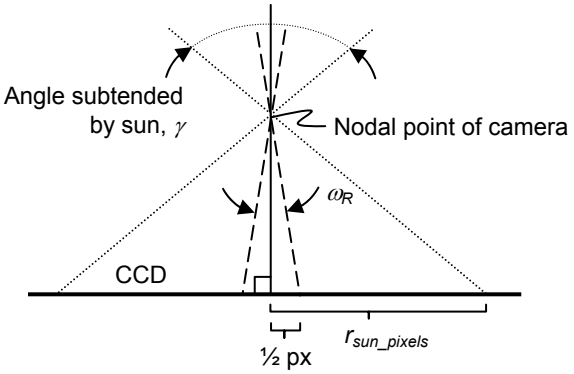

Figure 3. Determination of ω_R by comparison of angles projected onto the CCD using the sun half-angle ($\gamma/2$) as a scaling factor.

Combining Eqs. (6) - (8) yields the following equation for the irradiance on a receiver element, $E_{R,i}$ [W/m^2] as a function of each pixel value, $V_{CCD,i}$ [volts/px^2]:

$$E_{R,i} = \frac{V_{CCD,i} E_{DNI}}{\rho_{R,i} \tan^2(\gamma/2)} \frac{\pi r_{sun\_pixels}^2}{\sum_{sun} V_{CCD\_sun,i}} \tag{10}$$

where the term $\sum_{sun} V_{CCD\_sun,i} \,/\, \pi r_{sun\_pixels}^2$ is equivalent to the average pixel value in the sun image. For the same camera and settings, this value can be calculated once and used for subsequent calculations of the receiver irradiance. The receiver reflectivity, $\rho_{R,i}$, can be determined using methods described in Section 3.2.

3.2 Calculating Reflectivity

The average reflectivity of the receiver, ρ_R, in Eq. (10) can be determined by calibrating the reflectivity to yield a known integrated power irradiated on the receiver from a heliostat (or facet), assuming no spillage occurs from the receiver. This ensures conservation of energy in the predicted flux map, and the method can be carried out as follows:

1. Measure or estimate reflectivity of heliostat or facet, ρ_h, that will be used to illuminate the receiver.
2. Take RAW photo of the heliostat or facet beam on the receiver. The entire beam must be visible in the photo with no spillage. For all photos, use appropriate neutral density filters to prevent saturation of the CCD.
3. Take RAW photo of the receiver without the beam. Use the same camera and camera settings (i.e. zoom, f/stop, shutter speed, etc.) as in step 2.
4. Take RAW photo of the sun using the same camera and camera settings.
5. Calculate the average receiver reflectivity using the equation derived below (accounting for attenuation factors of the neutral density filters in the pixel values).

Conservation of energy requires that if no spillage occurs, the power on the receiver, P_R [W], must equal the power reflected from the heliostat, P_h [W]:

$$P_R = P_h \tag{11}$$

The power reflected by the heliostat is given by:

$$P_h = E_{\mathrm{DNI}} A_h \rho_h \left(\hat{\mathbf{s}} \bullet \hat{\mathbf{n}}_h\right) \tag{12}$$

where A_h is the reflective area of the heliostat [m^2], ρ_h is the heliostat reflectivity, $\hat{\mathbf{s}}$ is the unit sun vector, and the heliostat unit normal $\hat{\mathbf{n}}_h$ bisects $\hat{\mathbf{s}}$ and the specular reflected vector $\hat{\mathbf{t}}_h$ as shown in Figure 4.

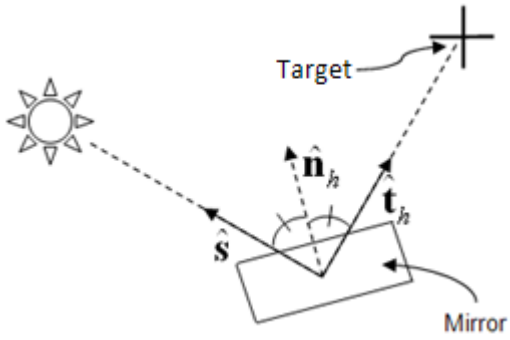

Figure 4. Schematic of vectors used to determine the cosine loss $\left(\hat{\mathbf{s}} \bullet \hat{\mathbf{n}}_h\right)$.

The total power irradiated on the receiver due to the heliostat beam is given by:

$$P_R = \sum_{\mathrm{beam}} E_{R,i} A_{R,i} \tag{13}$$

where $E_{R,i}$ [W/m^2] is the irradiance incident on a receiver surface element, $A_{R,i}$ [m^2], that is imaged by pixel i. The receiver surface element area, $A_{R,i}$, is given in Eq. (7). Eq. (10), which calculates $E_{R,i}$, is modified slightly to account for the ambient lighting, which may contribute to a non-negligible amount of the irradiance received on the receiver from only a single heliostat or facet (as opposed to a much larger irradiance from an entire heliostat field):

$$E_{R,i} = \frac{(V_{CCD,i} - V_{CCD,i\_ambient}) E_{DNI}}{\rho_{R,i} \tan^2(\gamma/2)} \frac{\pi r_{sun\_pixels}^2}{\sum_{sun} V_{CCD\_sun,i}} \tag{14}$$

where $V_{CCD,i}$ is the CCD pixel value at a single pixel on the photo of the receiver *with* the beam and $V_{CCD,i\_ambient}$ is the CCD pixel value at the same pixel on the photo of the receiver *without* the beam (only ambient lighting). Combining Eqs. (12) -(14) in Eq. (11) and assuming r and θ are approximately the same for all points on the receiver yields the average reflectivity for the receiver:

$$\rho_R = \frac{\pi r^2}{A_h \rho_h \left(\hat{\mathbf{s}} \bullet \hat{\mathbf{n}}_h\right) \cos(\theta)} \frac{\sum_{\text{beam}} \left(V_{CCD,i} - V_{CCD,i\_ambient}\right)}{\sum_{\text{sun}} V_{CCD\_sun,i}} \quad (15)$$

The method described above produces an effective reflectivity, ρ_R, for the entire receiver surface illuminated by the collector beam. If the reflectivity distribution on the receiver surface is highly variable, then a reflectivity distribution, $\rho_{R,i}$ must be determined to accurately calculate the incident irradiance on each surface element of the receiver, $A_{R,i}$, using Eq. (10). This can be done by imaging a coupon of known reflectivity in the field of view of the receiver image. Assuming the lighting conditions on the coupon and receiver are the same, the pixel values and reflectivity of the coupon can be used to scale the pixel values of the receiver and calculate the receiver reflectivity distribution, $\rho_{R,i}$:

$$\rho_{R,i} = \rho_C \frac{V_{CCD,i}}{\overline{V}_{CCD,C}} \quad (16)$$

where ρ_C is the coupon reflectivity, $V_{CCD,i}$ is the pixel value corresponding to the receiver element imaged by pixel i, and $\overline{V}_{CCD,C}$ is the average pixel value of the coupon image.

3.3 Perspective Views and Spatial Scaling

The method described in Section 3.1 converts CCD signals, V_{CCD}, for an image of a receiver into irradiance values on the surface of the receiver. The equations are valid for arbitrary receiver shapes, observer locations, perspectives, and distances.

After the irradiance distribution on the receiver is determined, some users might benefit from the added ability of using the flux image to measure the size, in meters, of a certain feature on the receiver. For a cylindrical receiver, a user may benefit from knowing the angular position along the receiver circumference that corresponds to a certain flux point of interest. Without further processing, the horizontal and vertical axes of the flux image are measured and plotted in pixels. However, equations can be derived that describe the conversion of these pixel-lengths on the horizontal and vertical axes of a flux image into spatial dimensions on the receiver, measured in meters or degrees [9].

In general, the meters-per-pixel conversion factor is not constant and is affected by the perspective of the camera. Suppose a photographer standing on the ground snaps a photograph of a receiver mounted on top of a tower. For the conversion of vertical pixels to meters along the height of the receiver, we must consider that the meters-per-pixel conversion factor for a pixel at the top of the photograph will be larger than at the bottom of the photograph. Similarly, for the conversion of horizontal pixels to meters along the width of a flat-panel receiver, the meters-per-pixel for a point closer to the camera will be smaller than for a point farther from the camera. For a cylindrical receiver, the center of the image will correspond to a smaller subtended angle (degrees) per pixel than at the edge of the image.

The effects of horizontal, vertical, and cylindrical perspectives on spatial scaling in the resulting flux maps have been addressed independently of each other and equations have been derived [9]. However, coupled effects from perspective views can exist. When a camera looks up at a tall object, the top of the object appears narrower than the base of the object. Similarly, when a camera looks along a wide object, the closer section of the object appears taller than far sections. To consider these coupled effects, each row and column of pixels in an image would need its own unique vertical and horizontal axis, respectively. When a camera is pointed up toward a tall cylinder, a horizontal plane through the cylinder surface projects an arc of an ellipse onto the camera. Each vertical position on the cylinder axis would need its own elliptical contour drawn on the image in order to honor this effect. These coupled effects were not considered in this study, but this only impacts the accuracy of the spatial scales used for the flux maps, not the irradiance distribution itself. The method described in Section 3.1 that converts CCD signals, V_{CCD}, into irradiance values on the surface of the receiver is still valid for arbitrary receiver shapes, perspectives, observer locations and distances.

3.4 Error Sources

The accuracy of the PHLUX method to determine the irradiance on a receiver from digital images depends on the accuracy of the quantities measured in Eq. (10). In particular, the camera response is assumed to be linear for different irradiances imaged by the CCD. Ulmer et al. [5] provide error estimates for camera linearity, noise (dark current, readout), and spectral influences, which can be caused by a non-constant filter transmission as a function of radiation wavelength. Each of these factors was estimated to cause an error of approximately ±0.5% for a single pixel value. Dark current values (pixel values when no irradiance exists on the CCD) were measured to be ~0.1% of the maximum pixel value for the Nikon D90 camera used in this study.

The attenuation factor of the neutral density filters is also expected to contribute errors to the measured irradiance. However, if the same filters are used to record the images of the sun and receiver, errors in the attenuation factors will cancel out in the calculation of the receiver irradiance (Eq. (10)) and reflectivity (Eq. (15)). In this study, filters had to be used to record images of the sun, but they were removed to record images of the single-heliostat beam on the tower. Although the

attenuation factor of the filters reported by the manufacturer may not be exact (especially across the solar weighted spectrum), errors in the attenuation factor are accounted for in the calculation of the receiver reflectivity in Eq. (15). If errors exist in the attenuation factor, the *effective* reflectivity calculated by Eq. (15) may be greater or less than the actual reflectivity of the receiver.

The PHLUX method also assumes that the receiver is a Lambertian reflector. Errors in Lambertian properties of the target were estimated by Ulmer et al. [5] to cause errors in pixel values ranging from -2% to 5%. Other estimates were provided by Ulmer et al. [5] to account for calibration and evaluation errors. The maximum total error was estimated to be approximately 10%. The error associated with the PHLUX method is likely to be similar since similar methods are used. Studies are being performed to evaluate the errors during actual testing and analyses using the PHLUX method.

4. TESTING AND ANALYSES

The PHLUX method was used to calculate the irradiance distribution from a heliostat beam on a central receiver tower at the National Solar Thermal Test Facility at Sandia National Laboratories in Albuquerque, NM. The heliostat (14E3) was positioned to reflect the sunlight onto the front of the central receiver tower as shown in Figure 5. The concentrated beam was centered on a water-cooled Vatell Thermogage flux tranducer (accuracy ±3%) so that the measured peak flux could be compared with the predicted peak flux using the PHLUX method. The front of the tower is painted white and is expected to behave like a Lambertian surface. The reflectivity of the front surface of the tower was determined using the method outlined in Section 3.2. Table 1 provides a summary of the test conditions and parameters.

Figure 5. PHLUX testing using heliostats at the National Solar Thermal Test Facility at Sandia National Laboratories, Albuquerque, NM.

Table 1. Summary of test conditions and parameters.

Date and Time:	1/18/2011 11:08 AM (MST)
Direct normal irradiance (W/m^2)[1]:	980
Position of heliostat east of tower (m):	24.4
Position of heliostat north of tower (m):	195
Slant range between camera and beam image on the tower (m):	358
Position of beam above heliostat pivot point (m):	25
Area of heliostat reflective surface (m^2):	37
Reflectivity of heliostat[2]:	0.95
Heliostat cosine loss $\left(\hat{\mathbf{s}} \bullet \hat{\mathbf{n}}_h\right)$:	0.95
Neutral density filter attenuation factor for beam image:	1
Neutral density filter attenuation factor for sun image:	8192
Calculated effective reflectivity of tower surface from Eq. (15):[3]	0.24

[1]Measured using Eppley pyrheliometer
[2]Measured using Device and Services reflectometer
[3]The calculated effective reflectivity ensures conservation of energy between the energy from the heliostat and the energy reflected by the tower. The value can include errors in the filter attenuation factor, DNI, and other factors used in the calculation of the receiver irradiance and may therefore be greater than or less than the actual tower reflectivity.

Figure 6 shows images of the heliostat beam and the sun taken using a Nikon D90 digital camera. These images were processed using the method described in Section 3.1. The resulting flux map is shown in Figure 7. The light-colored circle that appears within the beam image results from the presence of an annulus formed by a circular plate that covers a circular opening (approximately 0.6 m (2 ft) in diameter) for the flux transducer. The flux transducer is positioned in the center of the cover plate.

Figure 6. Images of the heliostat beam on the tower (left) and of the sun (right) taken with a Nikon D90. Both images were taken using the same camera settings (300 mm zoom, F/32, 1/4000 s). The sun image was taken using Tiffen neutral density filters.

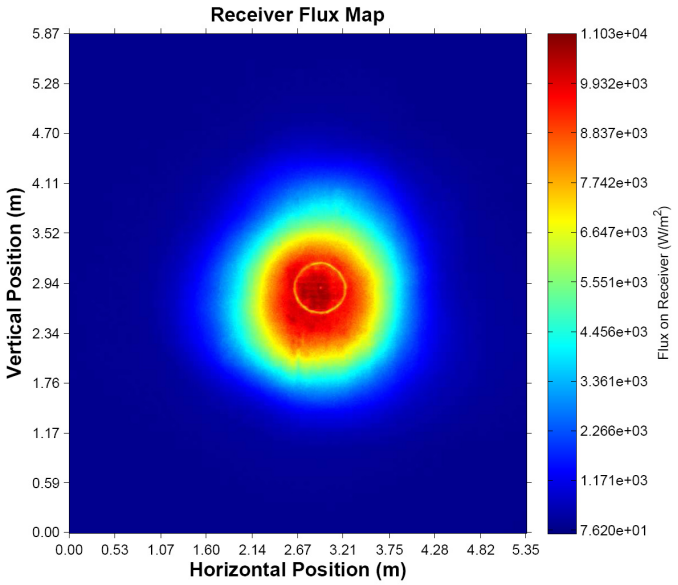

Figure 7. Irradiance distribution of heliostat beam on tower calculated using the PHLUX method.

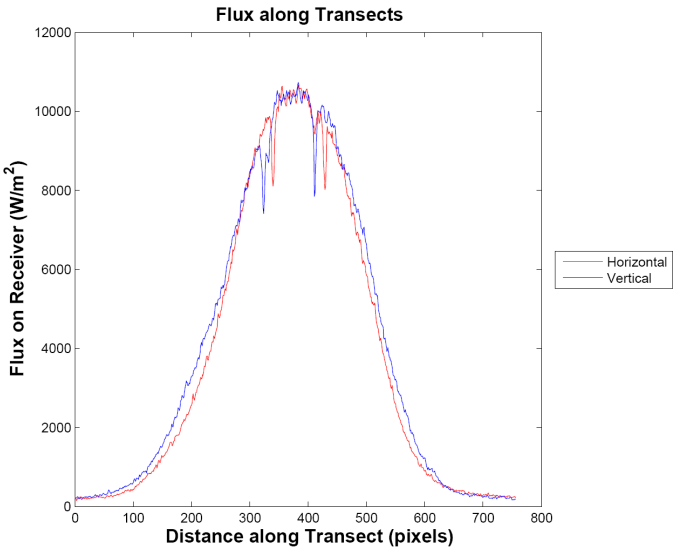

Figure 8. Irradiance distribution along vertical and horizontal transects centered within the heliostat beam on the tower.

The calculated irradiance along vertical and horizontal transects is plotted in Figure 8. The impact of the annulus on the calculated irradiance along the transects is clearly seen as a sharp decrease in the irradiance. An average reflectance was used in the calculation, but the actual reflectance for points corresponding to the annulus would be lower, which would produce higher irradiance values according to Eq. (10). Otherwise, the irradiance plot reveals a fairly smooth distribution (noise-to-signal ratio is low), indicating that using an average reflectivity value for the tower face was adequate. If the flux distribution was "noisy," this would indicate the need to calculate a distribution of reflectivity values as described in Section 3.2.

The peak flux is calculated by taking the average of the peak flux values corresponding to 102 pixels along the vertical and horizontal transects (pixels 350-400) in Figure 8. The calculated peak flux is 10.4 kW/m^2. The measured peak flux using the Vatell Thermogage flux tranducer (accuracy ±3%) was 10.2 kW/m^2. The relative error between the measured and predicted peak flux using the PHLUX method was 2%. Additional tests are being conducted to determine flux distributions with different heliostats and multiple heliostats to further evaluate the PHLUX method.

5. CONCLUSIONS

A new method is described to determine flux distributions on receivers and targets from heliostats or other collectors for concentrating solar power applications. The method uses a CCD camera (similar to previous methods), but it does not require additional sensors, calorimeters, or flux gauges on the receiver or target. It can accommodate high solar fluxes and spillage from the receiver. The only additional information required besides the digital images recorded from the CCD camera is the direct normal irradiance and the reflectivity of the receiver. Methods are described to calculate either an average reflectivity or a reflectivity distribution for the receiver using the CCD camera. The novel feature of this new PHLUX method is the use of recorded images of the sun to scale both the magnitude of each pixel value and the subtended angle of each pixel.

A test was performed to evaluate the PHLUX method using a heliostat beam on the central receiver tower at the National Solar Thermal Test Facility at Sandia National Laboratories in Albuquerque, NM. Results showed that the PHLUX method was capable of producing an accurate flux map of the heliostat beam with an error in the peak flux of 2% relative to a flux-gauge measurement. Additional tests are being performed to determine the flux distribution for different heliostats and multiple heliostats to evaluate the PHLUX method.

ACKNOWLEDGMENTS

The authors would like to thank Cheryl Ghanbari and Ed Smith for their assistance with the heliostat beam testing.

Sandia National Laboratories is a multi-program laboratory managed and operated by Sandia Corporation, a wholly owned

subsidiary of Lockheed Martin Corporation, for the U.S. Department of Energy's National Nuclear Security Administration under contract DE-AC04-94AL85000.

NOMENCLATURE

A	Area [m^2]
d_{sun}	Distance between the earth and sun [km]
$d\Omega$	Solild angle subtended by the camera iris at the receiver element [sr]
E_{DNI}	Direct normal irradiance [W/m^2]
E_R	Irradiance at the receiver [W/m^2]
E_{CCD_W}	Irradiance on CCD pixel [W/px^2]
CCD	Charge coupled device
DNI	Direct Normal Irradiance [W/m^2]
I_N	Radiant intensity reflected normal to receiver [W/sr]
$\hat{\mathbf{n}}_h$	Unit vector normal to heliostat surface
P	Power [W]
PHLUX	Photographic Flux mapping method
px	Unit length of a pixel on the CCD
r	Distance between camera iris and receiver element being imaged by pixel i
r_{sun}	Radius of the sun [6.96×10^5 km]
r_{sun_pixels}	Number of pixels along the radius of the sun image in the CCD
$\hat{\mathbf{s}}$	Unit vector pointing to the sun
$\hat{\mathbf{t}}_h$	Unit vector of specular reflection pointing toward receiver
V_{CCD}	Response of the CCD (pixel value) in arbitrary voltage units [$volts/px^2$]
$V_{CCD\_ambient}$	Value of pixel i on the receiver with ambient lighting only (no beam)
V_{CCD_sun}	Value of pixel i in the sun image [volts]

Subscripts

C	Coupon
h	Heliostat
R	Receiver
i	Corresponding to pixel i
I	Camera iris

Greek Symbols

ρ	Reflectivity
ϕ	Azimuth angle [rad]
γ	Angle subtended by the sun [~0.0093 rad]
θ	Angle between receiver surface normal and camera, zenith angle [rad]
ω_R	Angle subtended by receiver element imaged by pixel i

REFERENCES

[1] Mavis, C.L., 1988, "10 MWe Solar Thermal Central Receiver Pilot Plant Heliostat and Beam Characterization System Evaluation November 1981 – December 1986," SAND87-8003, Sandia National Laboratories, Livermore CA.

[2] Strachan, J.W. and R.M. Houser, 1993, "Testing and Evaluation of Large-Area Heliostats for Solar Thermal Applications, SAND92-1381, Sandia National Laboratories, Albuquerque, NM.

[3] Blackmon, J.B., 1985, "Development and performance of a digital image radiometer for heliostat evaluation at Solar One, *J. Solar Energy Engr.*, 107, 315-321.

[4] Johnston, G., 1998, "Focal Region Measurements of the 20 m^2 Tiled Dish at the Australian National University," *Solar Energy*, 63(2), 117-124.

[5] Ulmer, S., W. Reinalter, P. Heller, E. Lupfert, and D. Martinez, 2002, Beam Characterization and Improvement with a Flux Mapping System for Dish Concentrators, *J. Solar Energy Engr.*, 124, 182-188.

[6] Slack, M., P. Meduri, and A. Sonn, 2010, "eSolar Power Tower Performance Modeling and Experimental Validation," in proceedings of SolarPACES 2010, Perpignan, France, September 21-24, 2010.

[7] Yogev, O., P. Gleckman, and M. Rozler, 2009, "High-Heat Solar Flux Scanner," in proceedings of SolarPACES 2009, Berlin, Germany, September 15-18, 2009.

[8] Naor, G., G. Goldwine, R. Hayut, O. Bibi, E. Silberstein, O. Chernin, Z. Auman, G. Kroyzer, and A. Ziskin, 2010, "Flux Measurement System Using IR Camera," in proceedings of SolarPACES 2010, Perpignan, France, September 21-24, 2010.

[9] Ho, C.K. and S.S. Khalsa, 2010, "A Method to Measure Reflected Solar Irradiance Using a Digital Camera," Sandia National Laboratories Technical Advance, SD-11722, Albuquerque, NM.

APPENDIX – SUBTENDED SUN ANGLE

The perceived subtended angle of the sun depends, in part, on the distance between the sun and earth. The earth is actually closest to the sun in early January (the perihelion) and furthest from the sun in early July (the aphelion). The following equation gives the subtended angle of the sun, γ [rad], as a function of the known radius of the sun, r_{sun} [km], and distance between the earth and sun, d_{sun} [km]:

$$\gamma = 2\arctan\left(\frac{r_{sun}}{d_{sun}}\right) \tag{17}$$

where the radius of the sun, r_{sun}, is 6.96 x 10^5 km, and the distance between the earth and sun, d_{sun}, ranges from approximately 1.47 x 10^8 km – 1.52 x 10^8 km. Figure 9 shows the calculated subtended sun angles from Eq. (17) (converted to milliradians) using distances provided by the online ephemeris tables from JPL (http://ssd.jpl.nasa.gov/?horizons). Atmospheric and scattering effects are neglected in the calculation. The maximum subtended angle (9.46 mrad) occurs when the earth is closest to the sun, and the minimum subtended angle (9.15 mrad) occurs when the earth is furthest from the sun. The mean subtended angle is ~9.3 mrad.

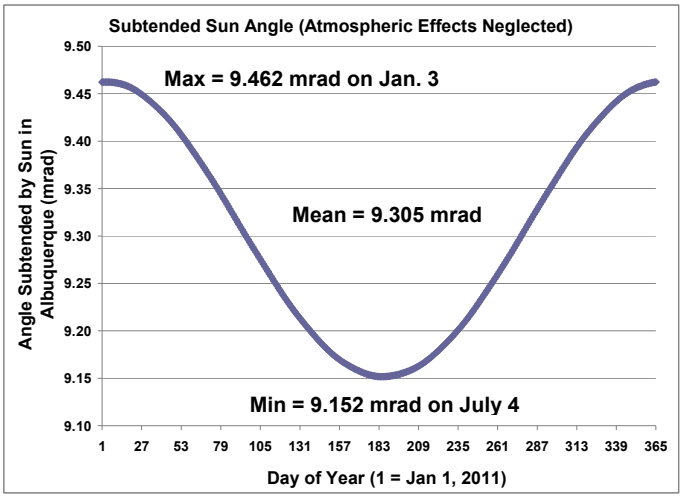

Figure 9. Subtended angle of the sun [mrad] as a function of day of year (for Albuquerque in 2011).